CHAPTER 7

Simulation and Experimental Result

Result from computer simulation and experimental testing are both described in this chapter. The simulation results are based on the numerical models of the test rig defined in chapter 4.

7.1 Numerical Analysis and Simulation Results

Appropriate parameter values for the rotordynamic model were determined using frequency response data for the rotor and stator structures, as obtained by impact tests described in Chapter 4. The state space model has a total of twelve states and includes first and second modes of vibration of the rotor with natural frequencies of 22 Hz and 75 Hz and damping ratios of 0.0023 and 0.0024 respectively. The stator is considered as a compliantly supported lumped mass with compliant rod supports, the stiffness of which can be varied.

7.1.1 Rotor-stator coupled whirl instability due to rotor natural mode

Dynamic behaviour of the rotor system during contact depends on structural dynamics of the rotor and the stator. This section will consider the situation where the stator dynamics have little influence over the operating frequency range. For this situation, the supporting rods for the stator are set to a short length so that the natural frequency of the stator is 120 Hz (exceeding the operating frequency range) and the corresponding damping ratio of the stator mode is 0.008. The contact stiffness for rotor-stator interaction κ depends on the radial stiffness of the force sensor, which is estimated to be 40 kN/m. This value of the radial stiffness will also be used as an upper limit for the contact stiffness, as required for the controller synthesis. The radial clearance between the contact disk and contact ring of the force sensing device is 0.6 mm. The dynamic compliance of the rotor-stator structure

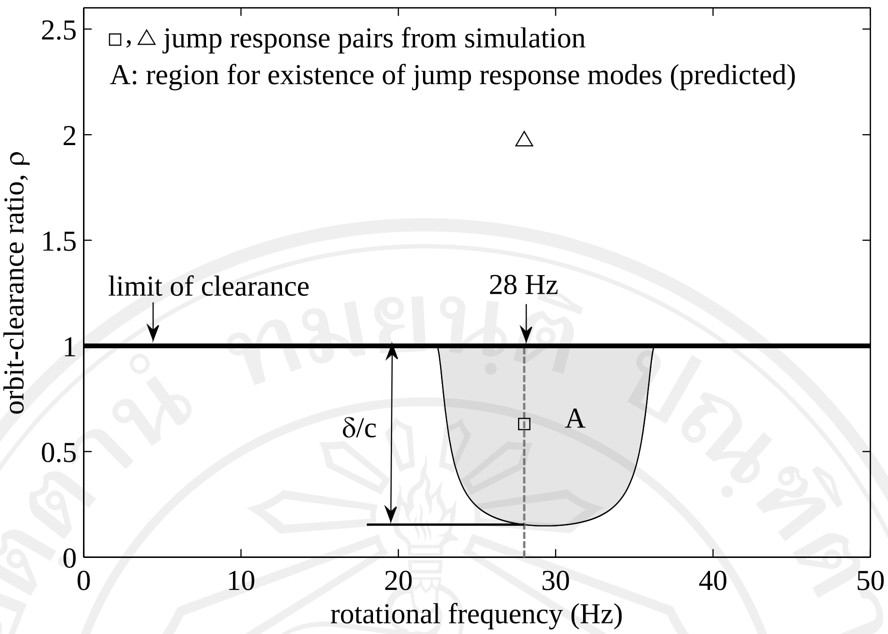

Figure 7.1: whirl mode map for test rig calculated from model which shows a jump response pair from simulation at operating frequency of 28 Hz with radial clearance of 0.6 mm

$H(\omega)$ can be calculate according to (5.2):

$$H(\omega) = \left[\begin{array}{cc} 1 & 0 \end{array} \right] \mathbf{T}(j\omega) \left[\begin{array}{cc} 1 & -j \end{array} \right]^T + k^{-1} \tag{7.1}$$

where $\mathbf{T}(j\omega) = \mathbf{C}(j\omega\mathbf{I} - \mathbf{A})^{-1}\mathbf{B}_f$.

The whirl mode map, determined from the conditions for existence of the alternative vibration response (5.3) and (5.4), can be plotted as shown in figure 7.1. When the orbit radius for steady state vibration response of the rotor falls into region A, there is a possibility of transition from the low amplitude vibration (linear vibration of the rotor) to the high amplitude vibration (the coupled vibration of the rotor-stator structure).

The jump response can be demonstrated by a time-step simulation shown in figure 7.2. The results are taken for steady operation at a rotational frequency of 28 Hz. The rotor unbalance disturbance d is initially at a low level so that the rotor vibration is well within clearance limits and also falls in region A of the whirl mode map (square marker in figure 7.1). A temporary increase in unbalance causes rotor-stator contacts that lead the rotor whirl to transgress into a coupled rotor-stator orbit with a high amplitude (triangle

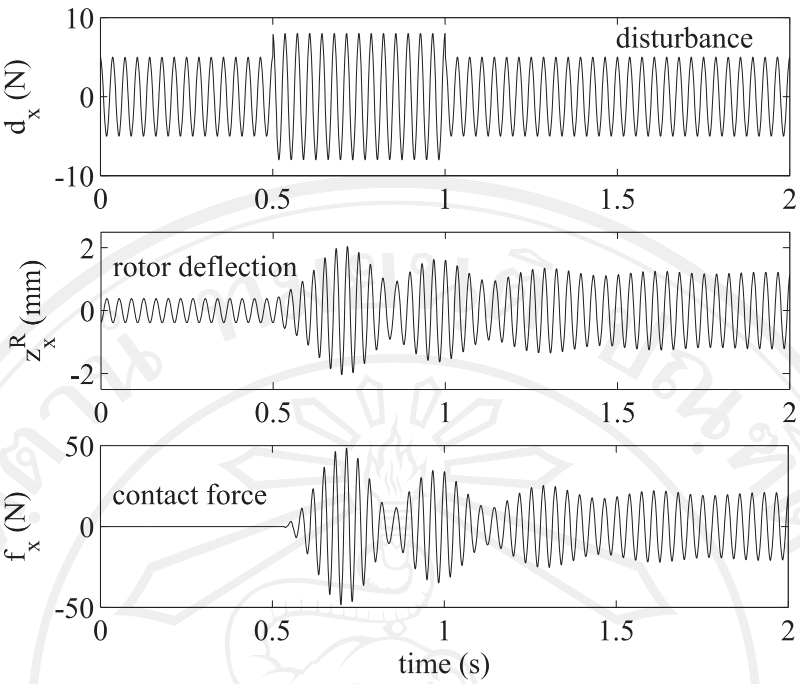

Figure 7.2: Transient response of the uncontrolled system due to temperary step change in disturbance at operating frequency of 28 Hz

marker in figure 7.1). After 0.5 seconds the disturbance returns to the original level, but the coupled whirl response persists indefinitely.

Controllers were synthesized using the methodology described in Chapter 6. A fixed operating frequency of 28 Hz was considered for the synthesis, as the potential for a jump response has already been determined according to figure 7.1 and figure 7.2. Predicted performance of the controllers can be seen from the "hysteresis plots" in figure 7.3. These show how the rotor vibration changes as the level of unbalance disturbance is slowly increased and then decreased. For the uncontrolled system, there is a large jump in amplitude when the orbit radius first exceeds the clearance. The jump response persists until unbalance returns to a low level. The interval where two possible response modes can occur is represented by δ. This corresponds to the vertical extent of region A, as shown in figure 7.1. Three difference controllers were synthesized with different values of the output weighting α, but using the same value for the contact stiffness bound of $\kappa = 40$ kN/m. All the controllers eliminate jump response behaviour for operation at 28 Hz and completely eliminate region A of the whirl mode map.

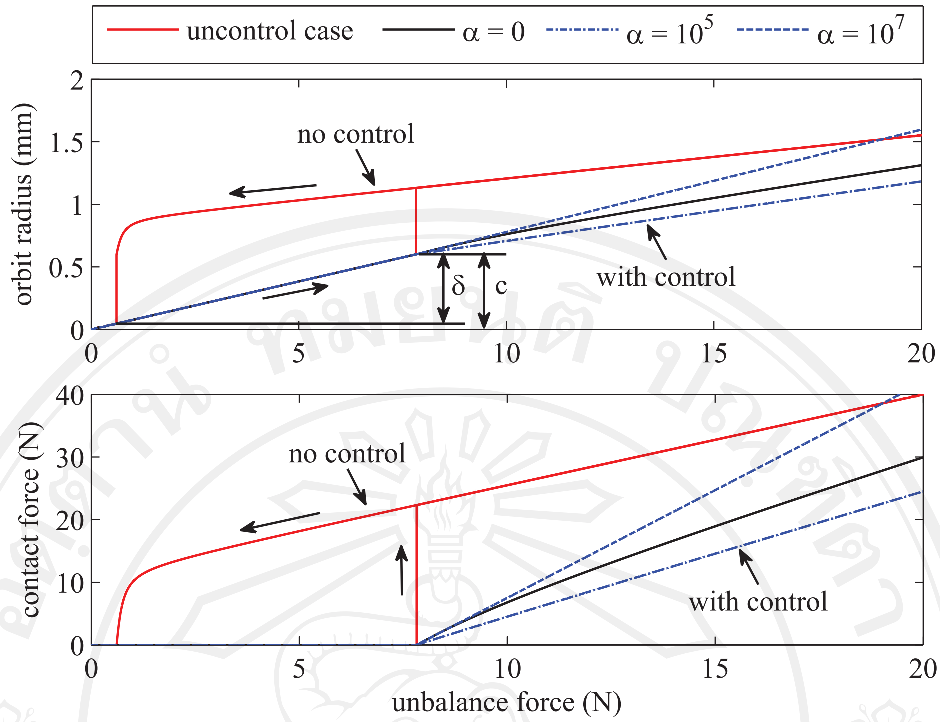

Figure 7.3: Variation of orbit radius and contact force with unbalance level for simulated steady state operation at 28 Hz

Figure 7.3 shows that the value of α used in controller synthesis influences the level of contact force when interaction occurs. To explain this influence, the basic equation for jump response prediction (5.1) may be considered. The existence of jump solution depends on the phase of $H(\omega)$. However, when contact is unavoidable ($\rho > 1$), the steady state contact force depends on the magnitude of $H(\omega)$. As the design weighting α is used to penalize $\|z\|$, increasing α tends to reduce the magnitude of $H(\omega)$ and thus gives larger contact forces.

The dynamic compliance magnitudes $|H(\omega)|$ for controller synthesized with different values of α are presented in figure 7.4. These are calculated from the transfer function matrix for the controlled system $\mathbf{T}(j\omega)$ as defined by $\mathbf{C}(j\omega\mathbf{I} - \mathbf{A} - \mathbf{B}_u\mathbf{K})^{-1}\mathbf{B}_f$. For the selected frequency, $|H(\omega)|$ is the highest with $\alpha = 10^5$, which is consistent with the results in figure 7.3. Although all these controllers have low pass properties, increasing α also tends to increase bandwidth and gain. In the proposed design procedure, α and k may be considered as design variables with suitable values selected by analysis and simulation. For the results presented in the remainder of this thesis, the controller designs are based on $\alpha = 0$

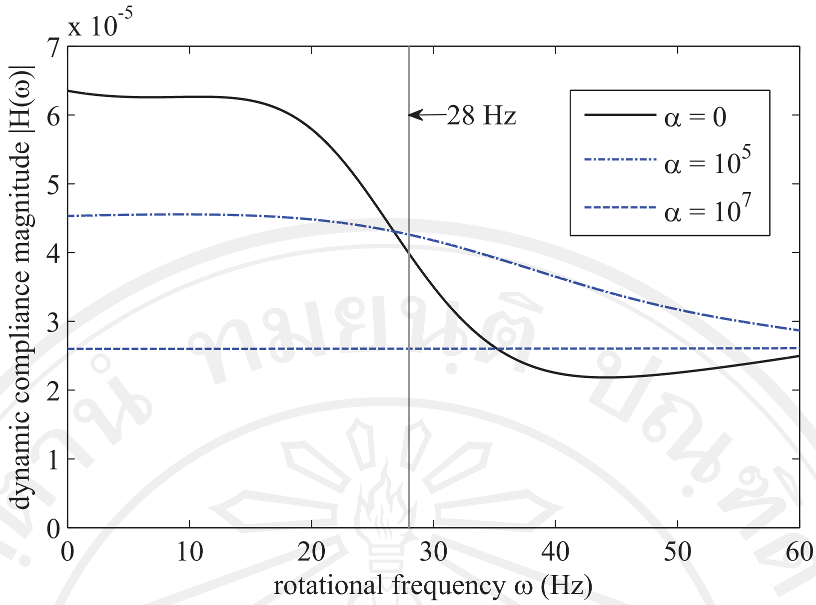

Figure 7.4: Dynamic compliance $H(\omega)$ for the controlled system. The design parameter α has an important influence on the magnitude of this function

and $k = 40$ kN/m.

In the controlled case, the transient response due to the same unbalance disturbance as in the uncontrolled case is shown in figure 7.5. These plots can be directly compared with figure 7.2. The jump response is prevented and the level of contact forces during interaction is greatly diminished.

When the initial vibration of the rotor is not in the region A, e.g. for operation at 38 Hz, then the amplitude jump behaviour no longer exists. Transient response of the uncontrolled system is shown in figure 7.6. Although a jump response does not occur there is a high contact force during interaction. A controller was synthesized for this rotational frequency and was implemented on the system in simulation. Figure 7.7 shows that the controlled response. The action of the controller is to reduce rotor-stator contact force during interaction. The advantages of the control method, not only in stabilizing the contact-free vibration of the rotor, but also reducing the contact force while the contact occurs is thus shown.

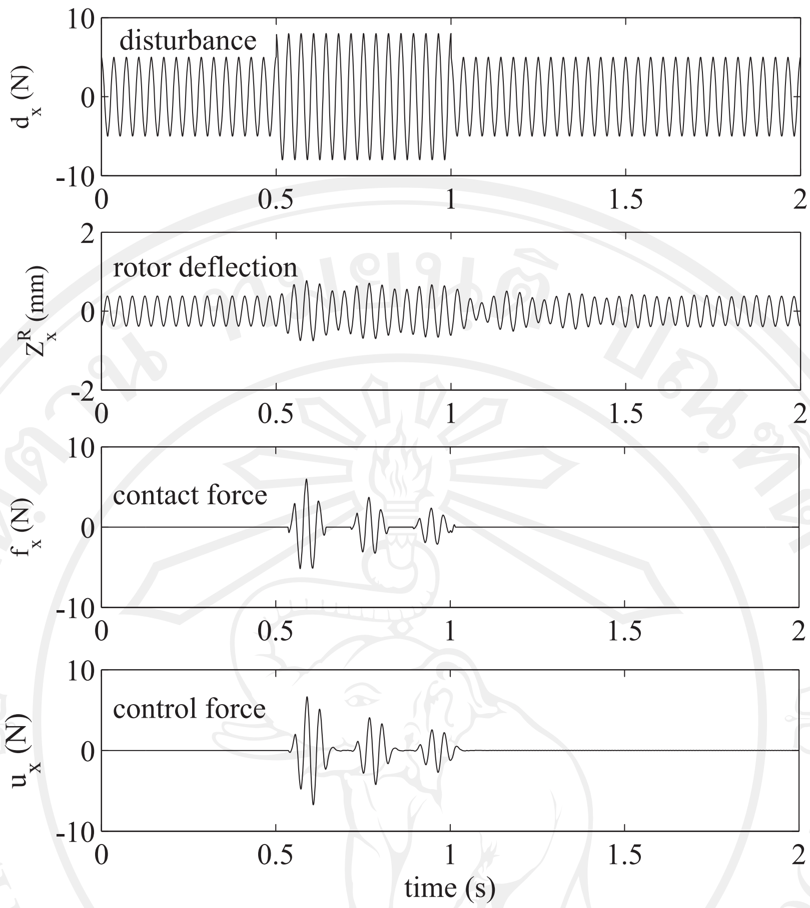

Figure 7.5: Transient response of the controlled system due to temperary step change in disturbance at operating frequency of 28 Hz

7.1.2 Rotor-stator coupled whirl instability due to stator natural mode

In this section it will be shown that the proposed control technique can deal with instability associated with structural modes of the stator, as well as the structural modes of the rotor. As control forces are not applied directly to the stator, the stator dynamics are not controllable by feedback. Nonetheless, the presence of the stator mode with natural frequency within the running speed range can lead to amplitude jump and coupled whirl. To investigate this issue, the natural frequency of the stator mode was decreased from 120 Hz to 30 Hz with damping ratio also changing to 0.07. The wirl mode map corresponding to this situation is shown in figure 7.8. There are two regions for possible jump response. The region A1 is associated with the rotor natural mode and the region A2 is associated

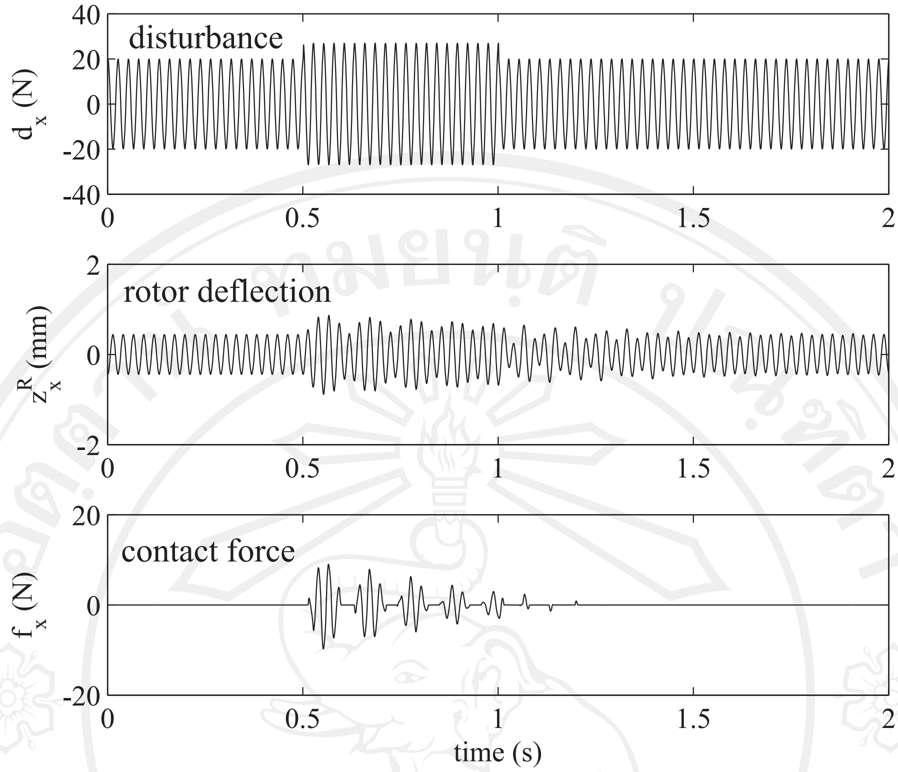

Figure 7.6: Transient response of the uncontrolled system due to temporary step change in disturbance at operating frequency of 38 Hz

with the stator natural mode.

Numerical simulations were performed for an operating frequency of 34 Hz. The rotor vibration due to unbalance disturbance was initially within clearance limits but with orbit size that falls in region A2 of the whirl mode map (square marker in figure 7.8). A temporary increase in unbalance causes a persistent jump response involving coupled whirl as shown in figure 7.9. Although the amplitude of rotor vibration does not change significantly, high amplitude vibration appears in the stator vibration and causes large contact force values.

The plots of the dynamic compliance $H(\omega)$ for the system are considered in order to obtain appropriate value for the weighting α and a suitable controller gain. The dynamic compliance magnitudes $|H(\omega)|$ for controller synthesized with different values of α are presented in figure 7.10. For the selected frequency of 34 Hz, $|H(\omega)|$ is the highest with

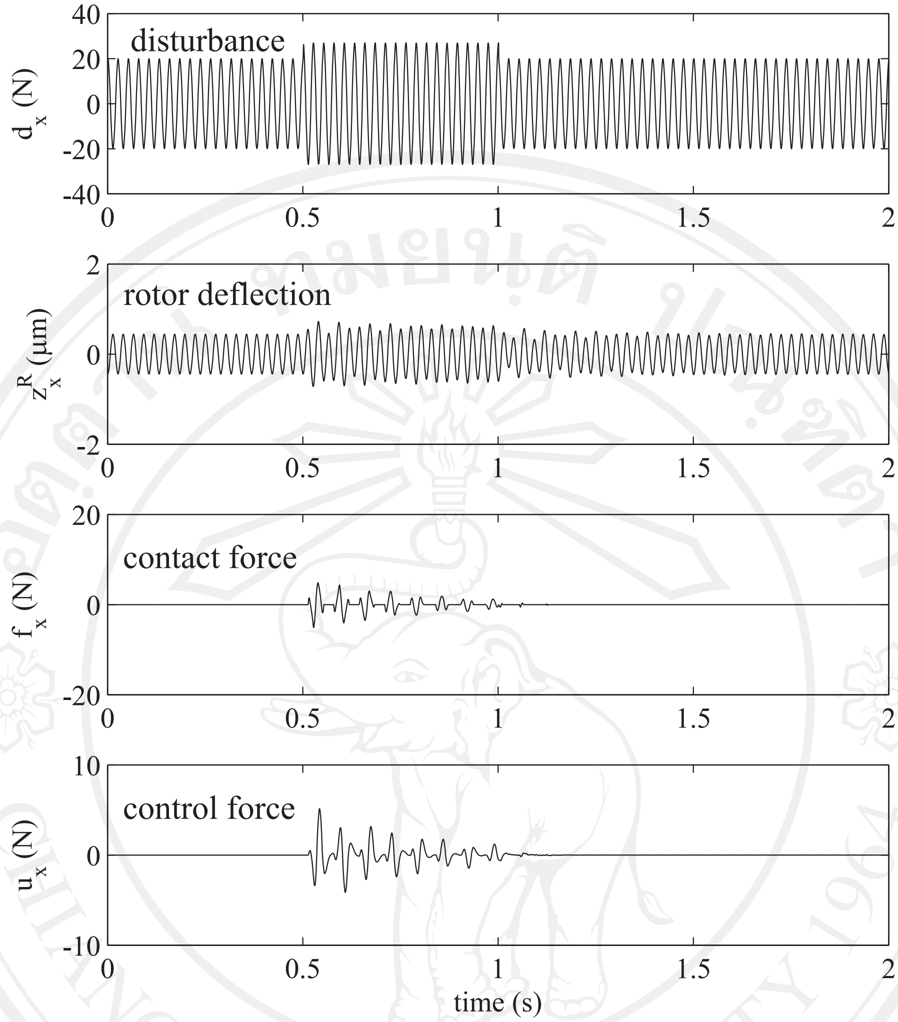

Figure 7.7: Transient response of the controlled system due to temporary step change in disturbance at operating frequency of 38 Hz

$\alpha = 0$. This implies that the controller with $\alpha = 0$ should give the lowest level of contact force, which is confirmed by the hysteresis plots in figure 7.11.

Therefore the controller was chosen for the modified system dynamic with $\alpha = 0$ and $k = 40$ kN/m. Simulation results confirm that with control, amplitude jump is prevented and the rotor returns to the original vibration state, as shown in figure 7.12. These results confirm that the controller design can deal with flexural modes associated with either the rotor or stator structure (or both).

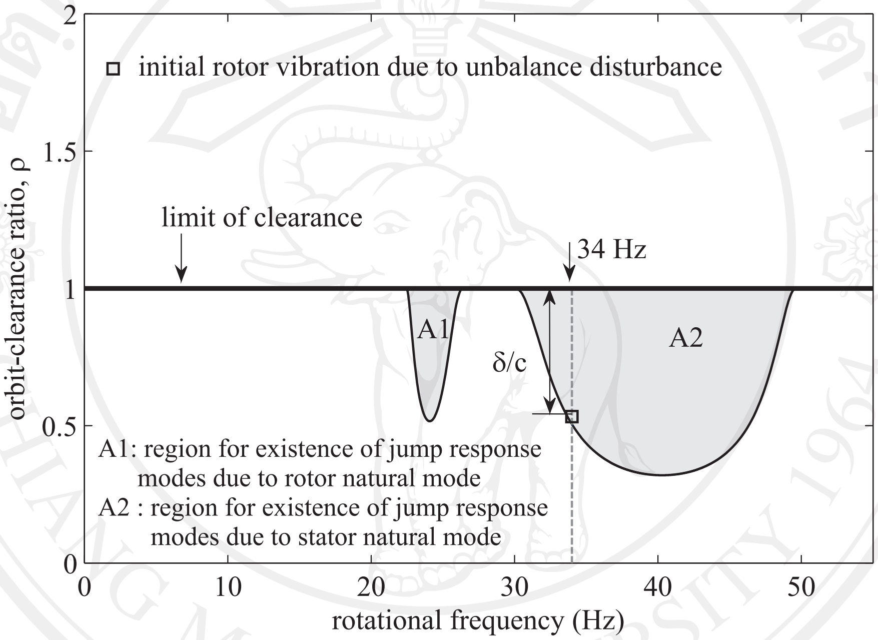

Figure 7.8: whirl mode map for test rig calculated from model which shows a jump response pair from simulation at operating frequency of 34 Hz with radial clearance of 0.6 mm

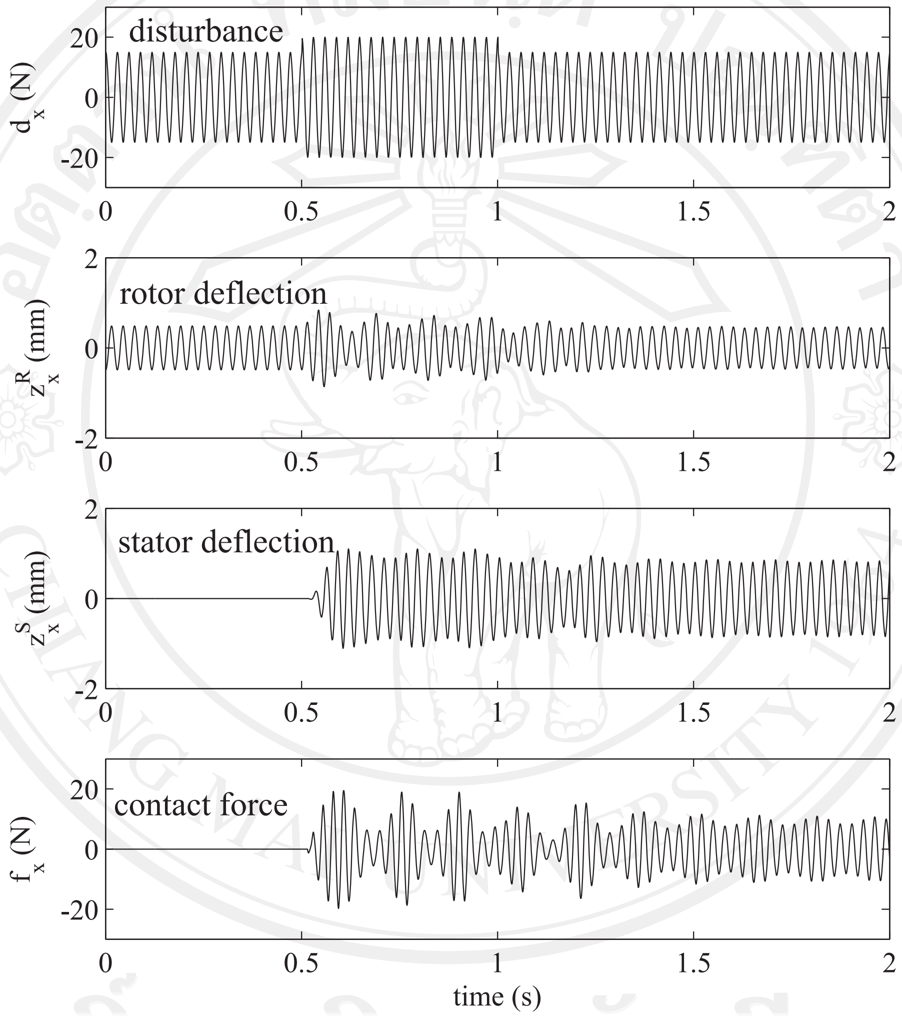

Figure 7.9: Transient response of the uncontrolled system due to temporary step change in disturbance at operating frequency of 34 Hz

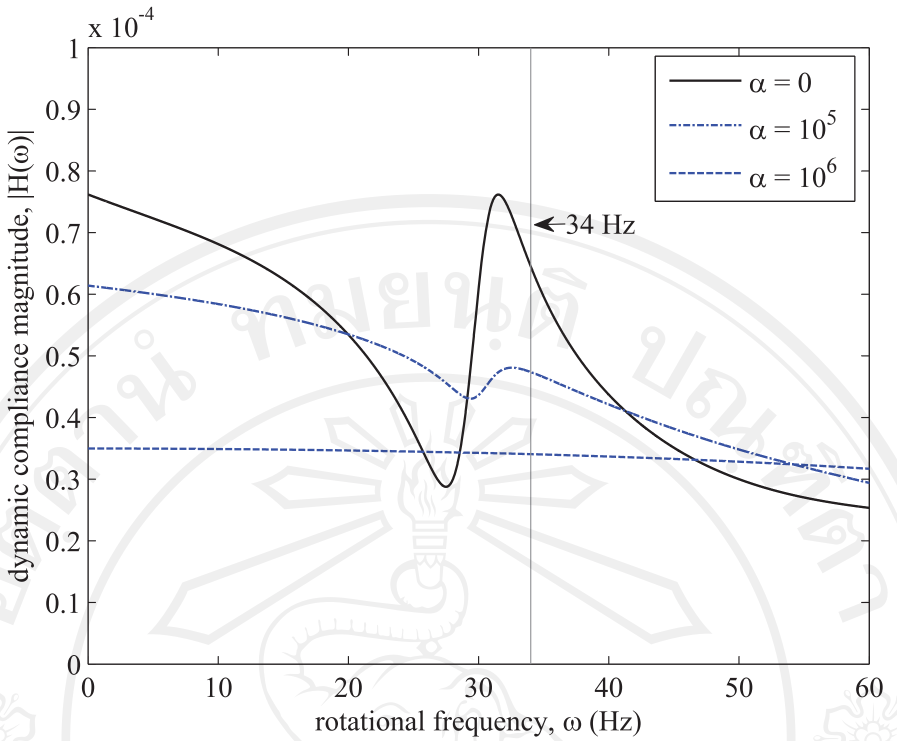

Figure 7.10: Dynamic compliance $H(\omega)$ for the controlled system with a flexible stator

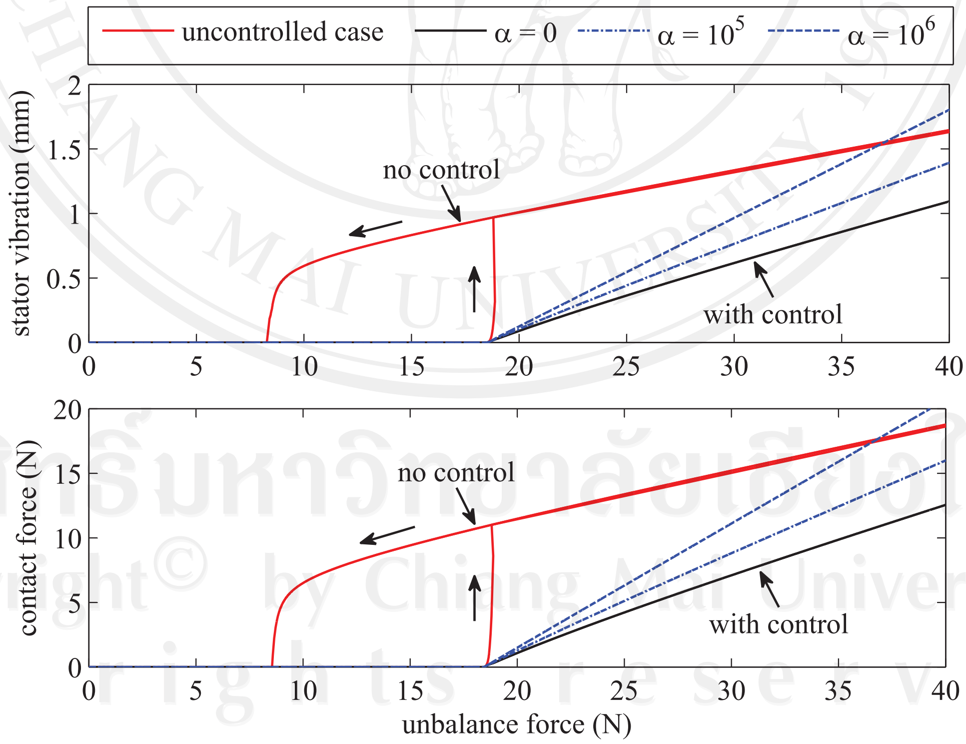

Figure 7.11: Variation of magnitude of stator vibration and contact force with unbalance level for simulated steady state operation at 34 Hz

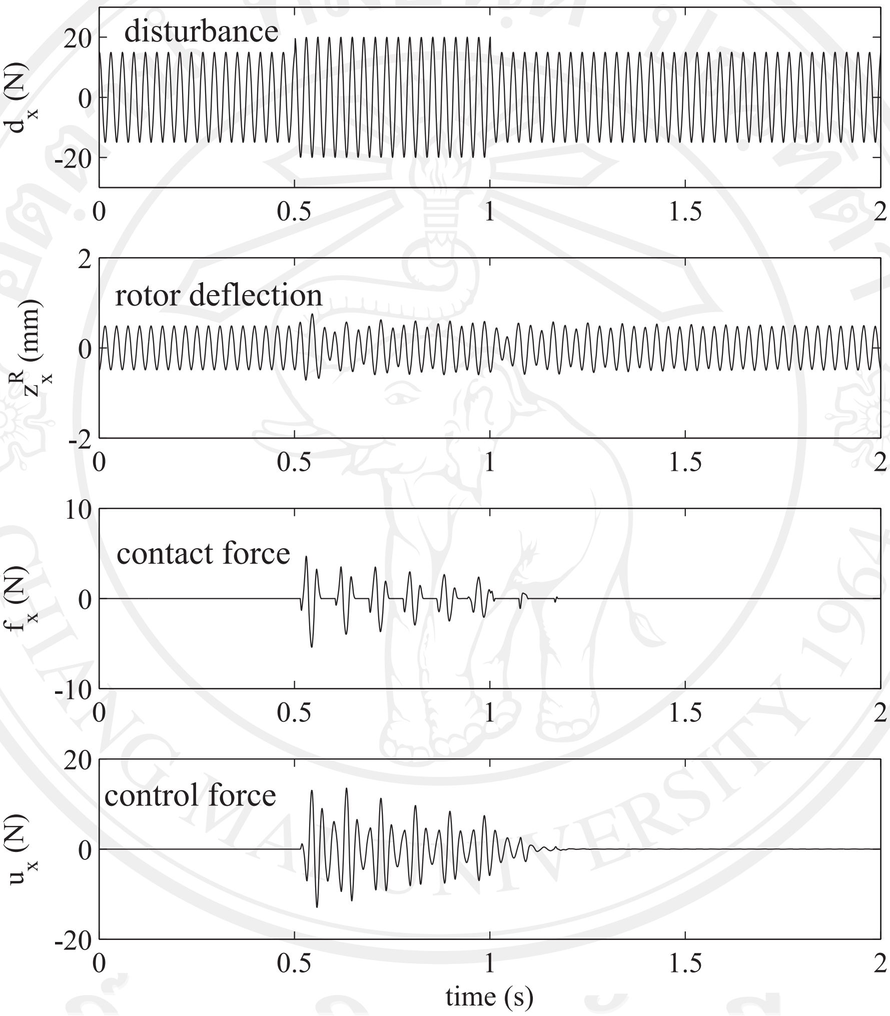

Figure 7.12: Transient response of the controlled system due to temporary step change in disturbance at operating frequency of 34 Hz

7.1.3 Backward whirl instability

The results in this section are based on a model of the form described in section 5.4 that takes account of the friction between the rotor and stator surfaces. The stiffness of 40 kN/m was used in the controller synthesis as an upper limit for contact stiffness. In this section, the natural frequency and damping ratio of the stator are set to 100 Hz and 0.008 respectively and the radial clearance limit is 350 μm.

The simulations are for a rotational frequency below the first natural frequency of the rotor. By simulating for an operating frequency of 15 Hz, the amplitude jump behaviour examined in the previous section is avoided. The boundary for possibility of backward whirl using the LMI conditions presented in chapter 5 are shown in figure 7.13. The region for possibility of backward whirl expands as the level of friction increases. For the uncontrolled system, the stability boundary predicted using the state space model is very similar to the boundary for possibility of a backward whirl solution from condition (2.21) for a single degree of freedom model (see figure 5.9). The gray area shown in figure 7.13 is the region where a backward whirl is possible.

Model parameters for point A ($k/\kappa = 0.55$,$\mu = 0.12$) are considered and also used for simulation. Figure 7.14 shows simulation results that demonstrate how a backward whirl can develop for the uncontrolled system. A step change in amplitude of a sinusoidal disturbance is considered here. Without control, a high contact force occurs and this leads to a limit-cycle whirl in the backwards direction. Figure 7.15 shows the plot of rotor orbit. The initial orbit of the rotor is contact-free as shown in figure 7.15a. The increase in the disturbance after 0.5 seconds causes the rotor to contact with stator. Friction between rotor and stator surfaces tends to drive the rotor to the reverse direction of rotation and it causes the bouncing motion as shown in figure 7.15b. Finally, the friction driven backward whirl progresses to a limit-cycle response with periodic bouncing, as shown in figure 7.15c.

The simulation for a higher friction case corresponding to point B ($k/\kappa = 0.55$,$\mu = 0.14$) was also undertaken. Figure 7.16 shows the transient response of the rotor due to a step change in disturbance. After contact begins a few seconds, the vibration of the rotor is

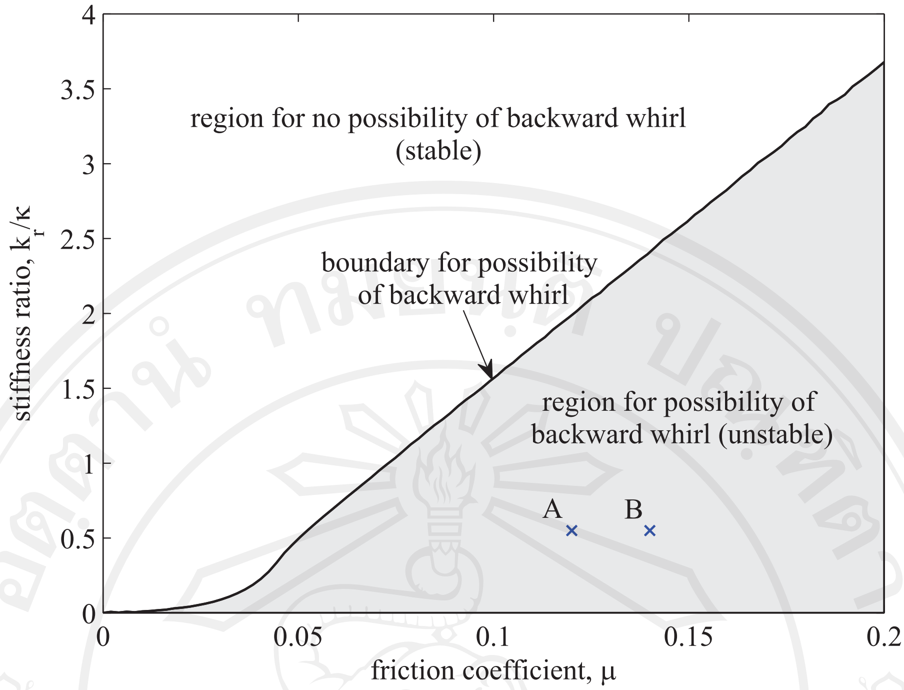

Figure 7.13: Boundary for possibility of backward whirl solution of the uncontrolled system using LMI stability conditions.

going unstable. Figure 7.17 shows how the rotor orbit grows from a contact free orbit to a fully-developed backward whirl. At the begining, the rotor orbit is in a contact-free state (figure 7.17a). An increase in disturbance causes initial rotor-stator contacts. At this stage the rotor orbit involves a bouncing motion driven by the friction force. Due to the higher friction coefficient for this case, the rotor orbit develops to a friction driven backward bouncing (figure 7.17c) which progresses to a fully-developed backward whirl, as shown in figure 7.17d.

To prevent the backward whirl instability, the controller is implemented on the rotor system model. The controller gain is synthesized for a value of $\alpha = 0$ because this value gives the highest value of $\|H(\omega)\|$ as shown in figure 7.18 and so this implies that the controller with $\alpha = 0$ should give the lowest level of contact force. Figure 7.19 shows the comparison of the boundaries for possibility of backward whirl between the controlled system and the uncontrolled system. The gray area is the region where the controller can eliminate the possibility of backward whirl. In the controlled case, the system with friction coefficient $\mu = 0.14$ is considered. Figure 7.20 shows transient response of the controlled system.

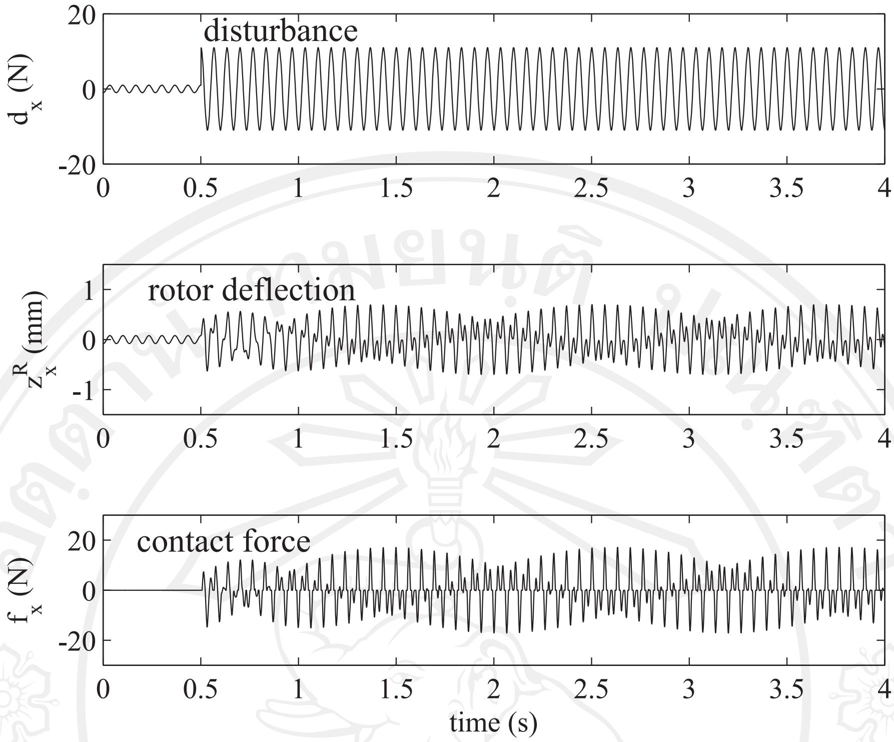

Figure 7.14: Transient response of the uncontrolled system with friction coefficient between rotor and stator surfaces $\mu = 0.12$ due to temporary step change in disturbance at operating frequency of 15 Hz

The control force applied through the magnetic bearing helps to reduce the contact force level and prevent whirl in the backwards direction. The orbit plot of the rotor in control case are shown in figure 7.21. Although the interaction between rotor and stator cannot be avoided, the controller can preserve a stable forward whirl as shown in figure 7.21c.

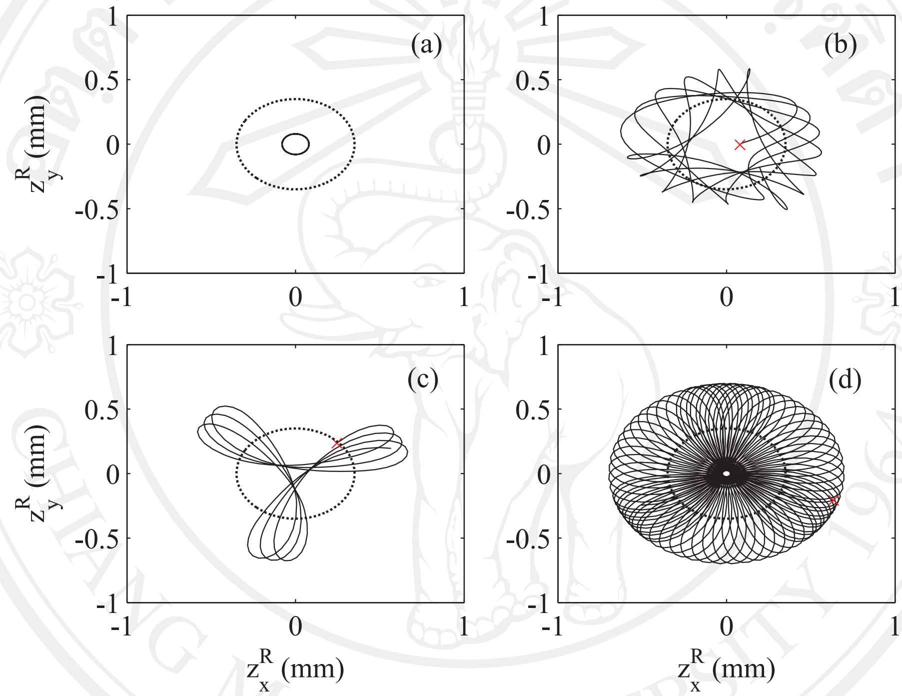

Figure 7.15: Orbit plots of contact disk at operating frequency of 15 Hz with friction coefficient between rotor-stator surfaces $\mu = 0.12$ (a) initial contact free orbit (b) rotor-stator rubbing transition orbit (c) limit cycle bouncing of friction driven whirl (d) limit cycle of friction driven whirl. An initial limit of clearance is indicated by a dotted circle.

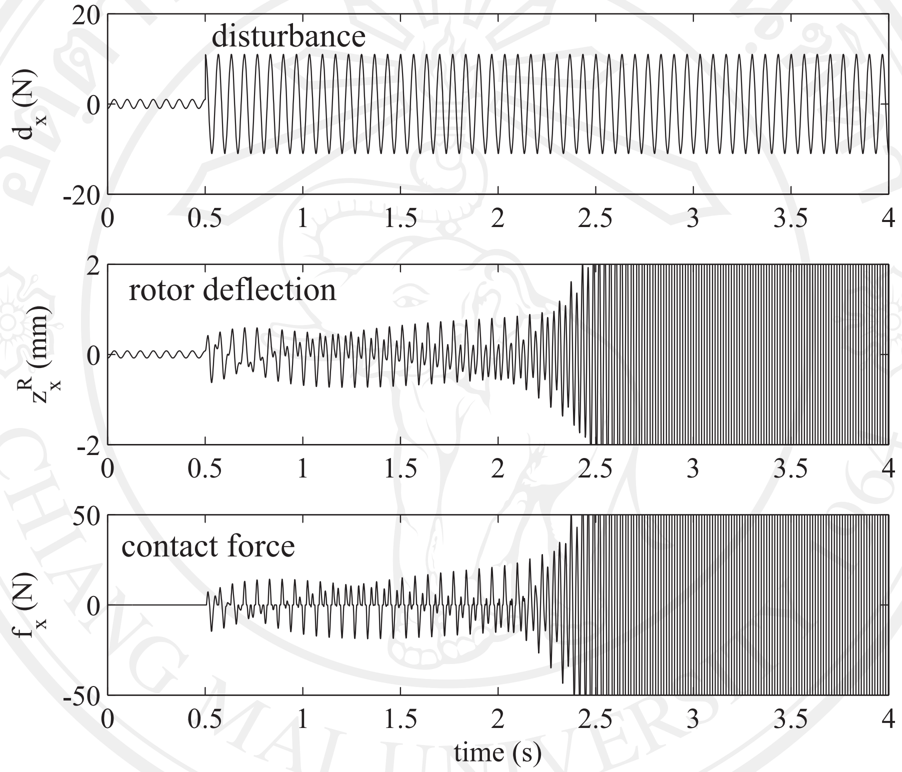

Figure 7.16: Transient response of the uncontrolled system with friction coefficient between rotor and stator surfaces $\mu = 0.14$ due to temporary step change in disturbance at operating frequency of 15 Hz

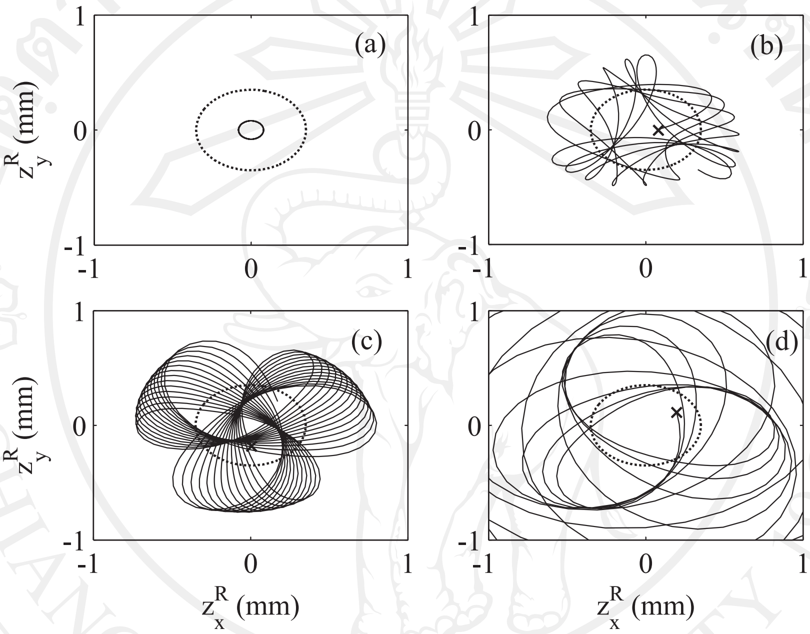

Figure 7.17: Orbit plots of contact disk at operating frequency of 15 Hz with friction coefficient between rotor-stator surfaces $\mu = 0.14$ (a) initial contact free orbit (b) rotor-stator rubbing transition orbit (c) rotor orbit is developed to friction driven backward bouncing (d) instability orbit of friction driven backward whirl. An initial limit of clearance is indicated by a dotted circle.

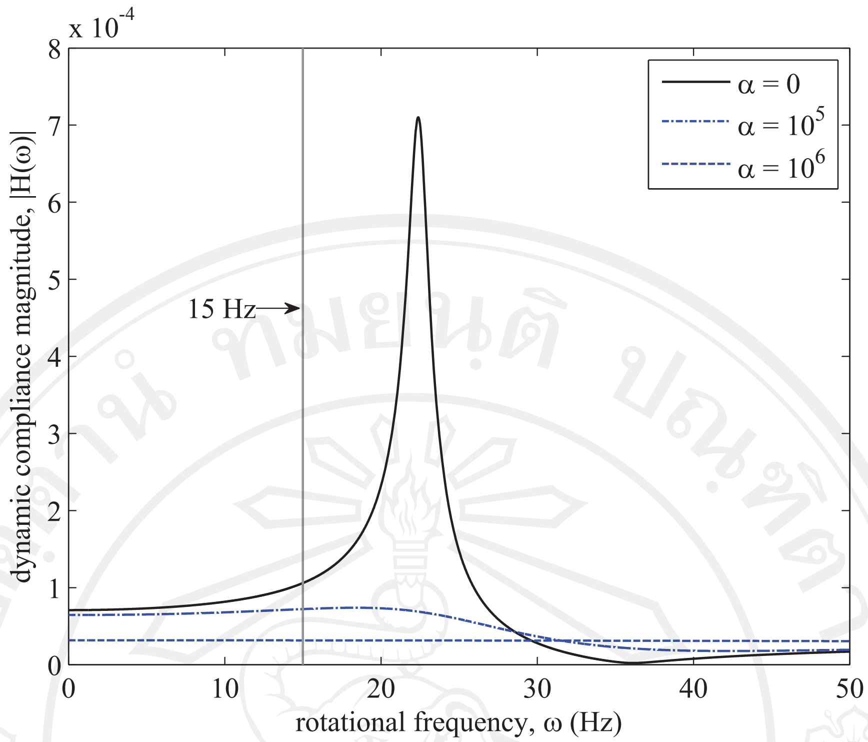

Figure 7.18: Dynamic compliance $H(\omega)$ plots for the controller gain selection with varying the desing parameter α

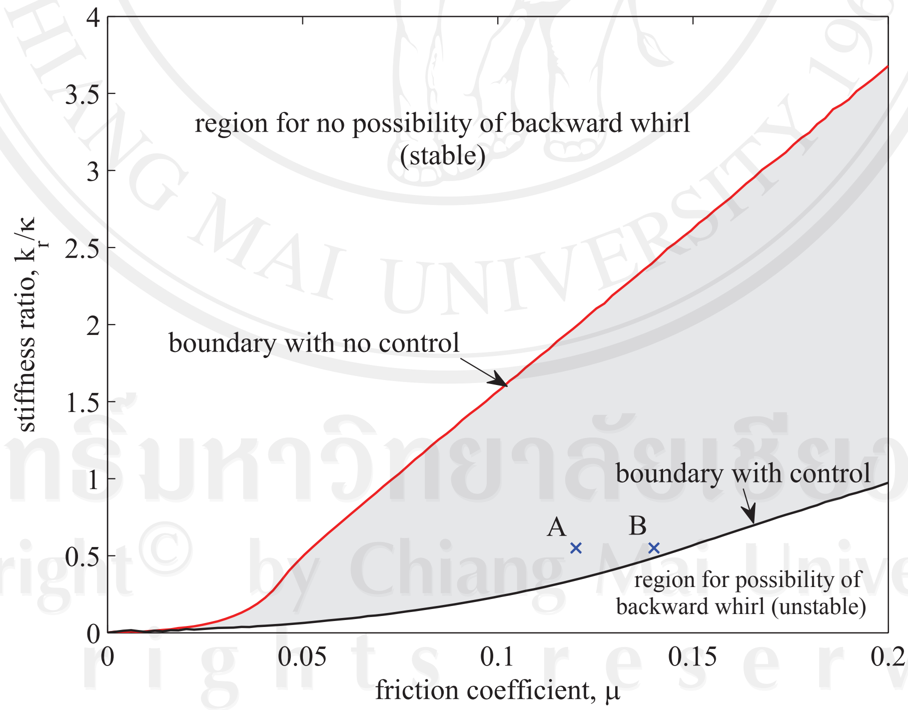

Figure 7.19: Comparison of boundary for possibility of backward whirl solution of the uncontrolled and controlled system using LMI stability conditions. The region where the controller can eliminate the possibility of backward whirl is indicated by the gray area.

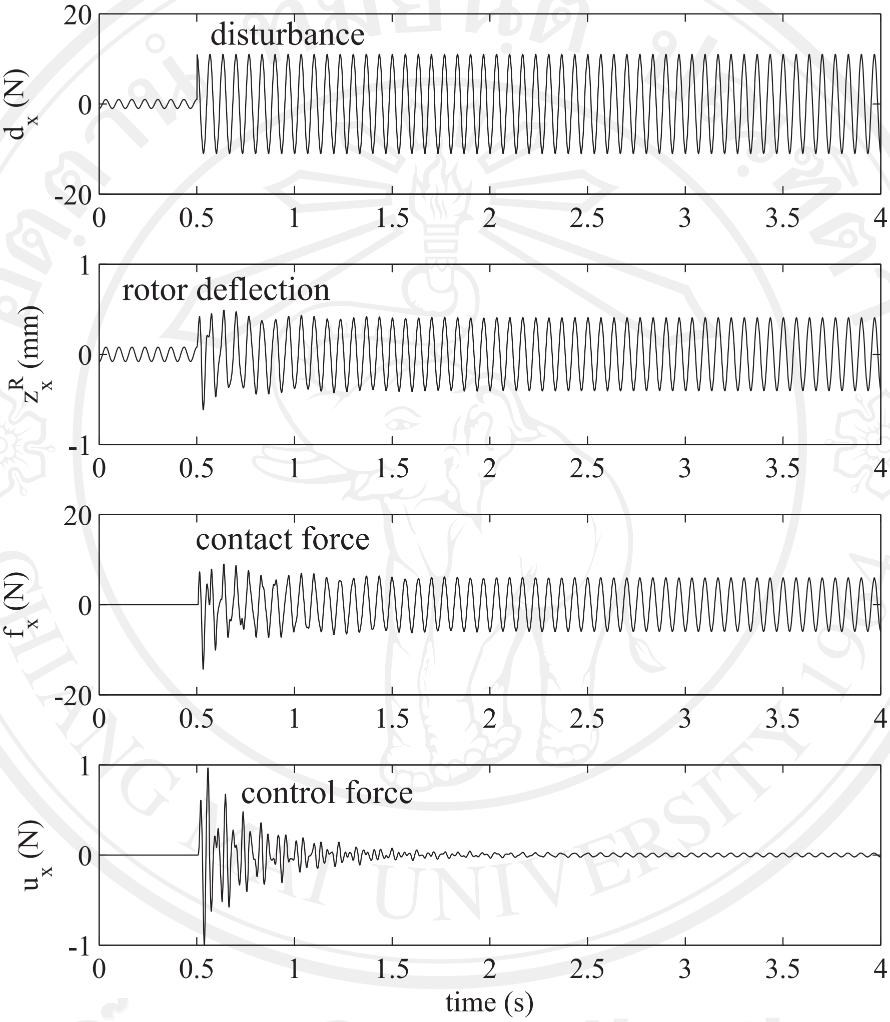

Figure 7.20: Transient response of the controlled system with friction coefficient between rotor and stator surfaces $\mu = 0.14$ due to temporary step change in disturbance at operating frequency of 15 Hz

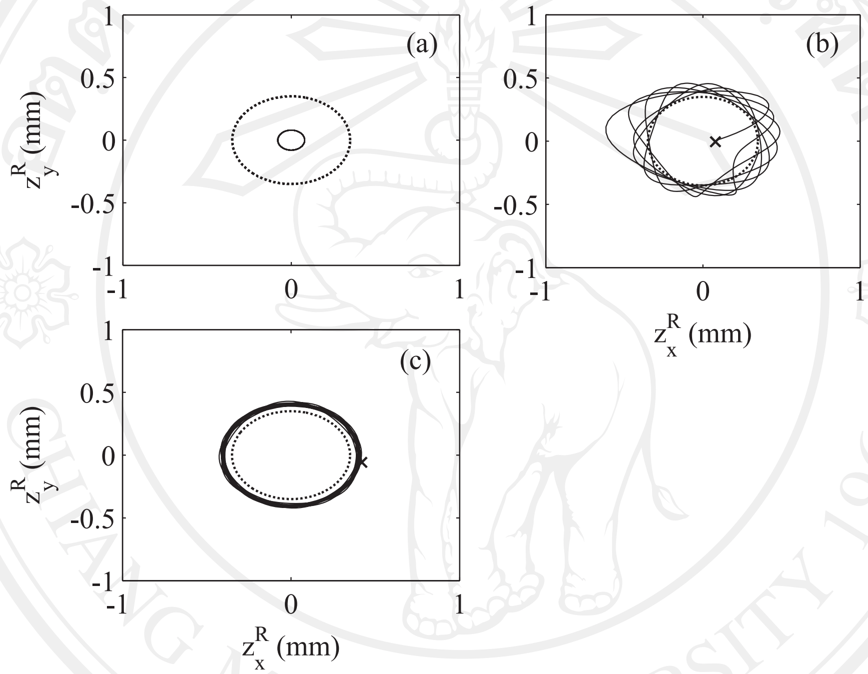

Figure 7.21: Orbit plots of contact disk of the controlled system at operating frequency of 15 Hz (a) initial contact free orbit (b) rotor-stator rubbing transition orbit (c) stable circular orbit of the rotor-stator rubbing case. An initial limit of clearance is indicated by a dotted circle.

7.2 Experimental Results

7.2.1 Rotor-stator coupled whirl instability due to rotor natural mode

Experimental results for identification of the hysteresis behaviour during increasing and decreasing unbalance are shown in figure 7.22. Separate graphs show uncontrolled and controlled cases. For these tests, the rotor is operating at a constant rotational frequency of 28 Hz and a simulated unbalance force is applied using the magnetic bearing. This acts in addition to the physical unbalance of the rotor. For the uncontrolled case shown in figure 7.22a, the interval for occurrence of a jump response δ is smaller than predicted but, over all, the results show reasonable agreement with the simulations in figure 7.3. The jump response can occur at low levels of excitation but causes high levels of contact forces. The results for operation with control show that the jump response is eliminated and that steady-state interaction forces are much lower (figure 7.22b).

Figure 7.23 and 7.24 show experimental results for transient response tests for uncontrolled and controlled cases respectively. They aim to replicate the time-step simulations of figure 7.2 and 7.5. In practice, the controller is effective in preventing a jump to the alternative whirl response that occurred without control. Discrepancies between the experimental and simulation results are believed to be mainly due to the non-isotropic properties of the experimental system. In particular, the magnetic bearing and force sensing device have a Cartesian structure that introduces some radial anisotropy. This causes fluctuations in the radial forces during rub between the rotor and stator, which is different to the smooth continuous rub seen in the simulation. An additional cause of inaccuracy may be the idealized nonlinear interaction model presented in section 4.4. It should be remarked, however, that the controller synthesis involves a robust approach in the sense that the exact model of the rotor-stator interaction is not used and this is a useful feature of the synthesis approach that may contribute to the good control performance seen in these experiments.

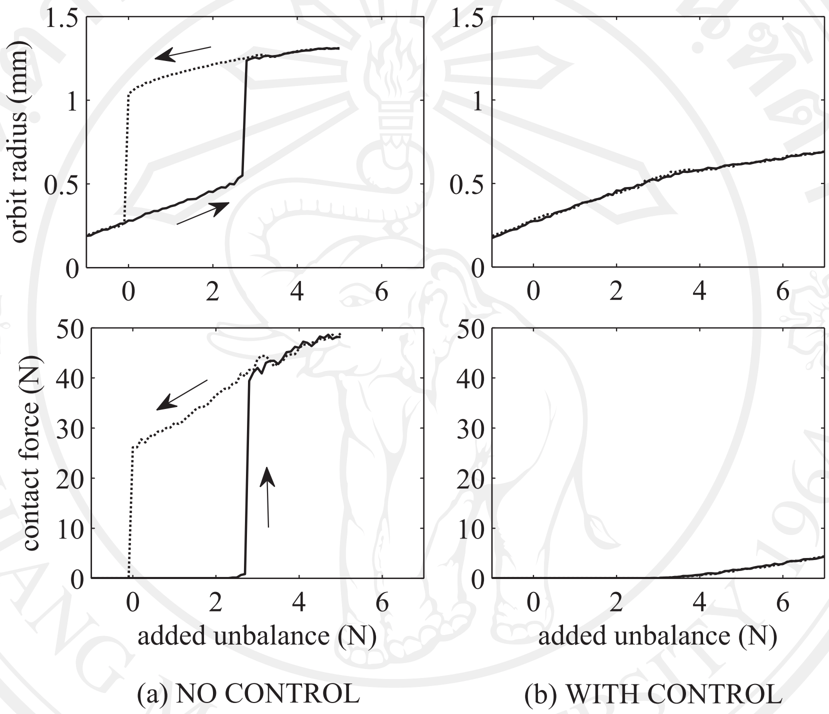

Figure 7.22: Variation of orbit radius and contact force with unbalance level for experiment with steady state operation at 28 Hz (a) Uncontrolled case. (b) Controlled case with $\alpha = 0$

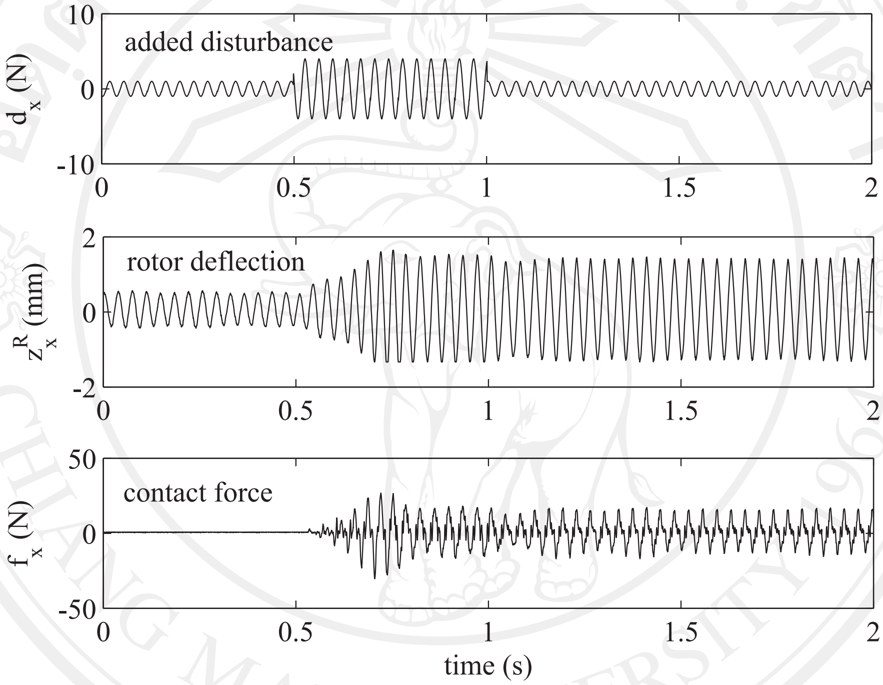

Figure 7.23: Experimental transient test at 28 Hz involving temporary increase in unbalance of uncontrolled case

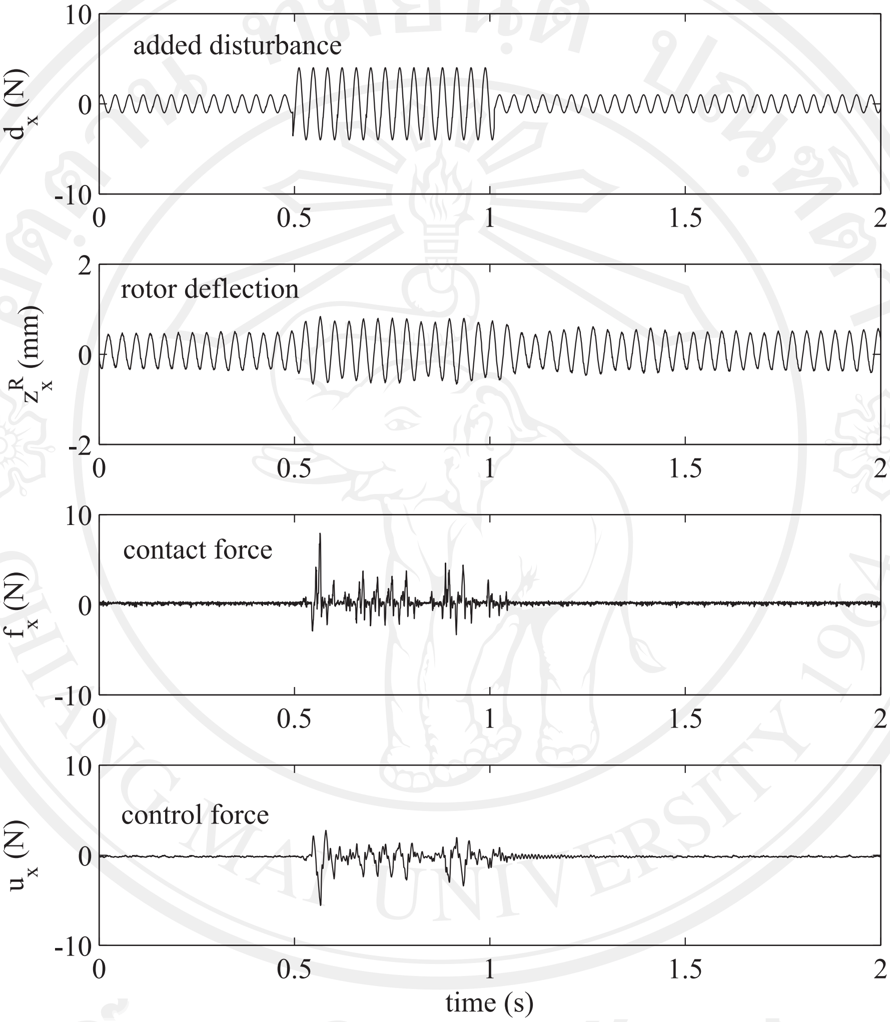

Figure 7.24: Experimental transient test at 28 Hz involving temporary increase in unbalance of controlled case

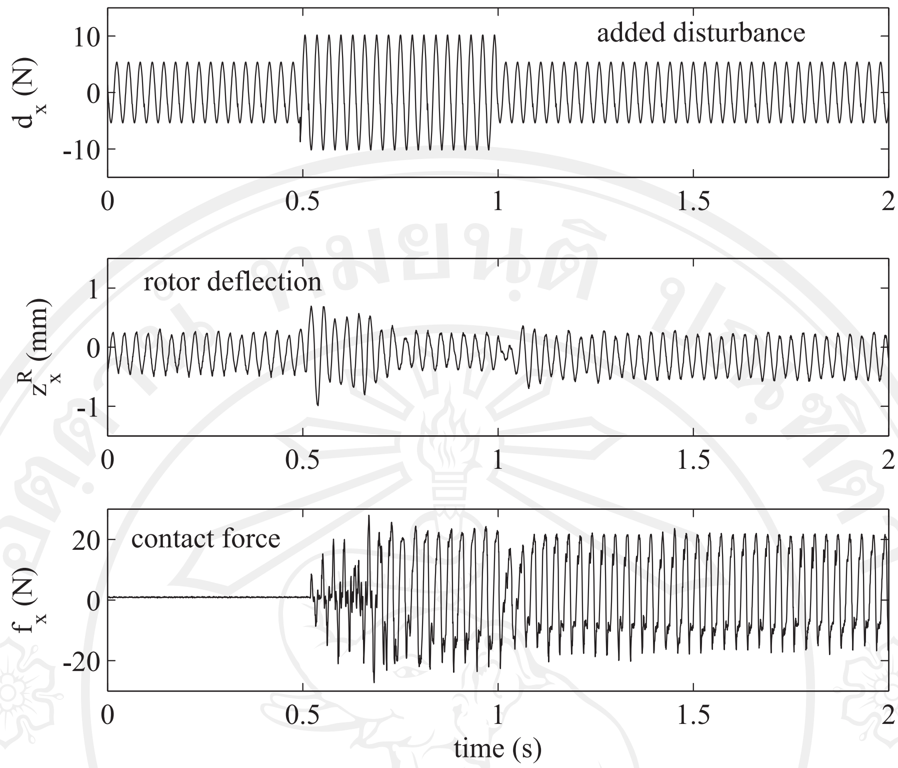

Figure 7.25: Experimental transient test at 34 Hz involving temporary increase in unbalance of uncontrolled case.

7.2.2 Rotor-stator coupled whirl instability due to stator natural mode

To obtain practical verification of the simulation results for the case of low frequency stator natural mode shown in section 7.1.2, the stator was modified by changing the support rods in order to decrease the natural frequency from 120 Hz to 30 Hz. Experiments were then undertaken at operating frequency of 34 Hz. The results are shown in figure 7.25 for an uncontrolled case and figure 7.26 for a controlled case. For the uncontrolled case, a temporary increase in unbalance causes a persistent jump response involving coupled whirl. Although the amplitude of the rotor vibration does not change significantly, high amplitude vibration of the stator causes large contact force values. With control, amplitude jump is prevented and the rotor returns to the original vibration state.

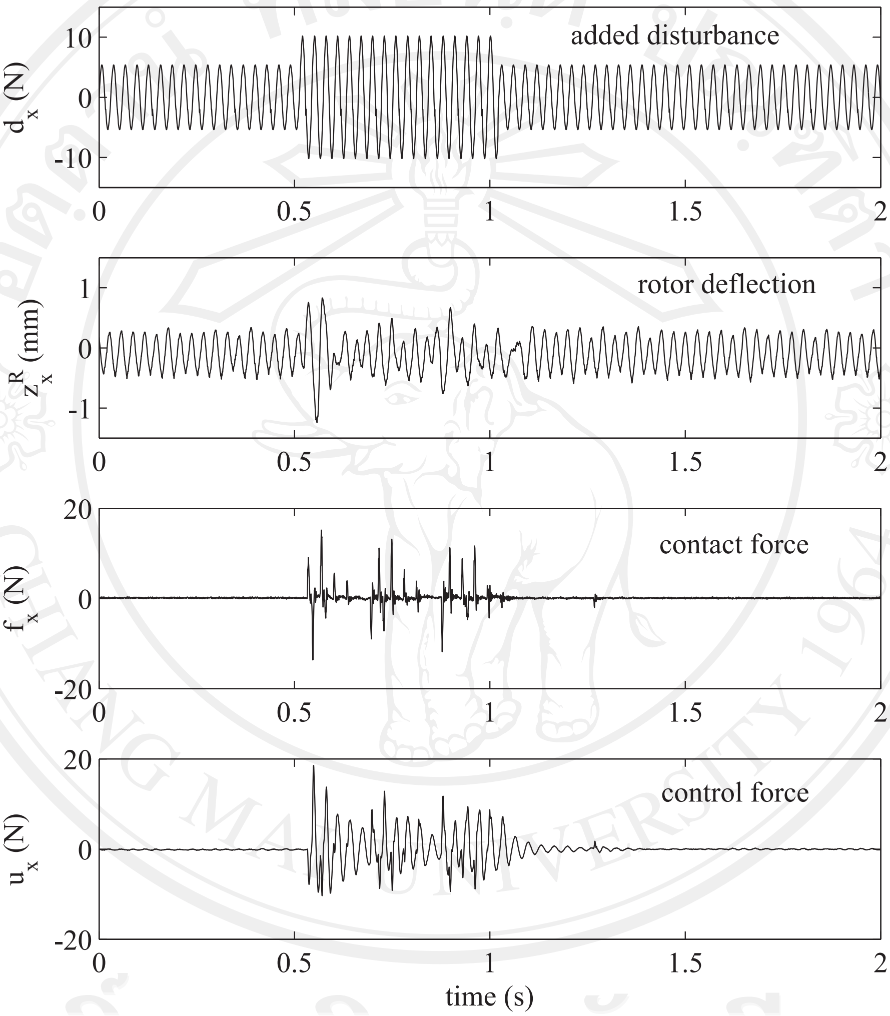

Figure 7.26: Experimental transient test at 34 Hz involving temporary increase in balance of controlled case.

7.2.3 Backward whirl instability

Experiments were undertaken to investigate possible backward whirl behaviour as demonstrated for the simulation model. These were performed for an operating frequency of 15 Hz, chosen to be below the first natural frequency of the rotor in order to avoid the amplitude jump behaviour. A thin sheet of sand paper was attached to the inner surface of the stator contact ring in order to increase the friction value for contact. The clearance space between the rotor and stator is therefore reduced to 0.35 mm. This set up corresponding to the simulated condition treated in section 7.1.3. The transient responses of the rotor due to step change in unbalance are shown in figure 7.27. When the unbalance disturbance is increased, contact between the rotor and stator occurs and generates the friction force that tends to drive the rotor whirl in the reverse direction to rotation as shown in figure 7.28b. Note that the contacting locations are moving in the reverse direction to rotation (clockwise) and this is considered to be an initial phase of a full backward whirl instability, as seen in the simulation results of section 7.1.3.

Figure 7.29 shows the transient response of the rotor due to the step change in disturbance as in the uncontrolled case. When contact is occurring, the rotational frequency of the rotor is decreased due to the friction force. This shows that the friction force still has an influence on the rotor whirl even with control. The orbit of the rotor in a controlled case is shown in figure 7.30. With control, the contacting locations are not moving and this result confirms that the control approach helps to inhibit a backward whirl behaviour. However, it is not possible to say how the controller would influence the occurrence of a fully developed backwards whirl as this could not be produced in the experimental system.

7.3 Summary

Controllers were synthesized using the model-based controller design approach described in the previous chapter. Simulation results were based on the numerical models of the test rig.

The simulation and experimental results in forward whirl case confirmed that the expected amplitude jump behaviour could occur at rotational frequencies above the rotor or stator natural modes. With control, the simulation results show that the amplitude jump due to both of the rotor and stator natural modes can be eliminated and this was also confirmed by the experiments. The level of contact force occurring with control depends on the value of the weighting parameter α used in the control synthesis. The lowest contact force level is given by the controlled system that has the highest dynamic compliance $H(\omega)$ as shown in the simulation.

The simulation results also showed the influence of the friction on the rotor system behaviour with two different values of the friction coefficient considered. With lower friction ($\mu = 0.12$), the rotor whirl response tended to a limit-cycle backward whirl with bouncing. With higher friction ($\mu = 0.14$), the contact force can lead the rotor whirl to an unstable backward whirl vibration with a perpetual growth in amplitude. With control, the stable forward whirl can be preserved. The experimental results did not show the same unstable vibration patterns seen in simulation but did indicate that an initial bouncing phase of backward whirl could be prevented by the controller.

Ideally, vibration behaviours involving fully developed backwards whirl would have been obtained by experiment. Difficulties in achieving this could possibly be due to energy dissipation effects that were not included in the simulation model. Changing (decreasing) rotor speed is another possible factor that was not included in the simulations.

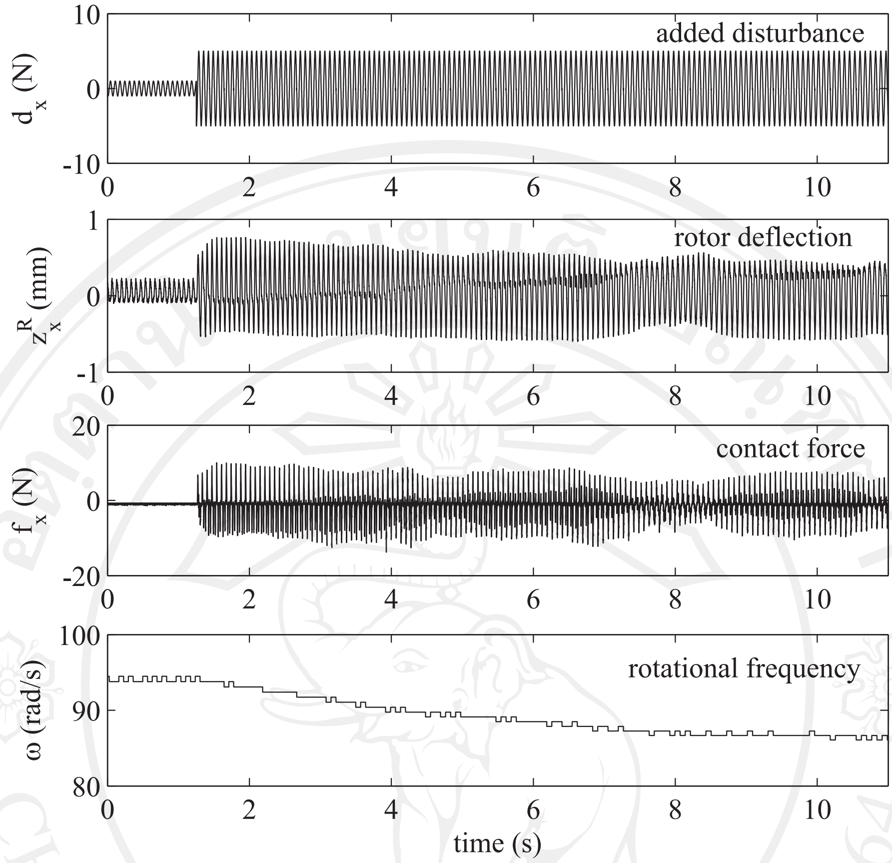

Figure 7.27: Experimental transient test at 15 Hz involving temporary increase in balance of uncontrolled case.

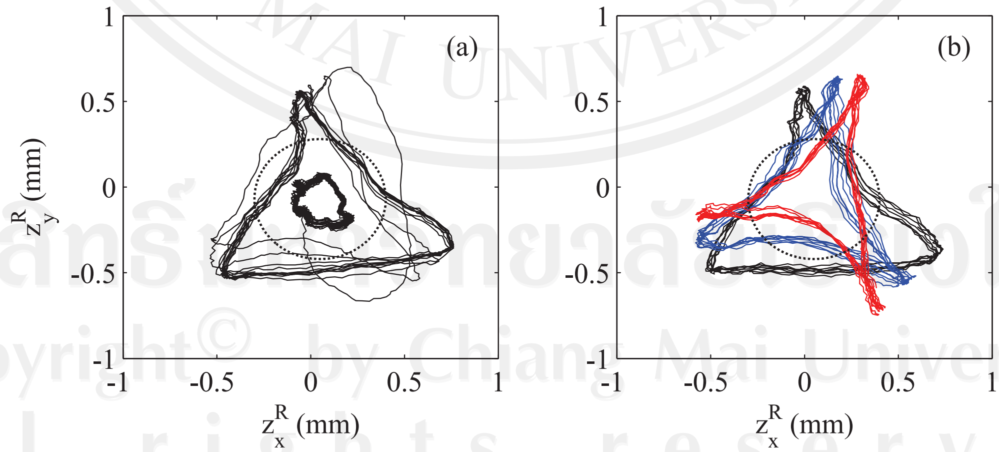

Figure 7.28: Rotor disk orbit at a contact plane operating at frequency of 15 Hz (a) Rotor orbit transition from contact free orbit to contact orbit. (b) Rotor orbit in second 2-2.5(black), second 5-5.5(blue) and second 10-10.5(red). An initial limit of clearance is indicated by a dotted circle.

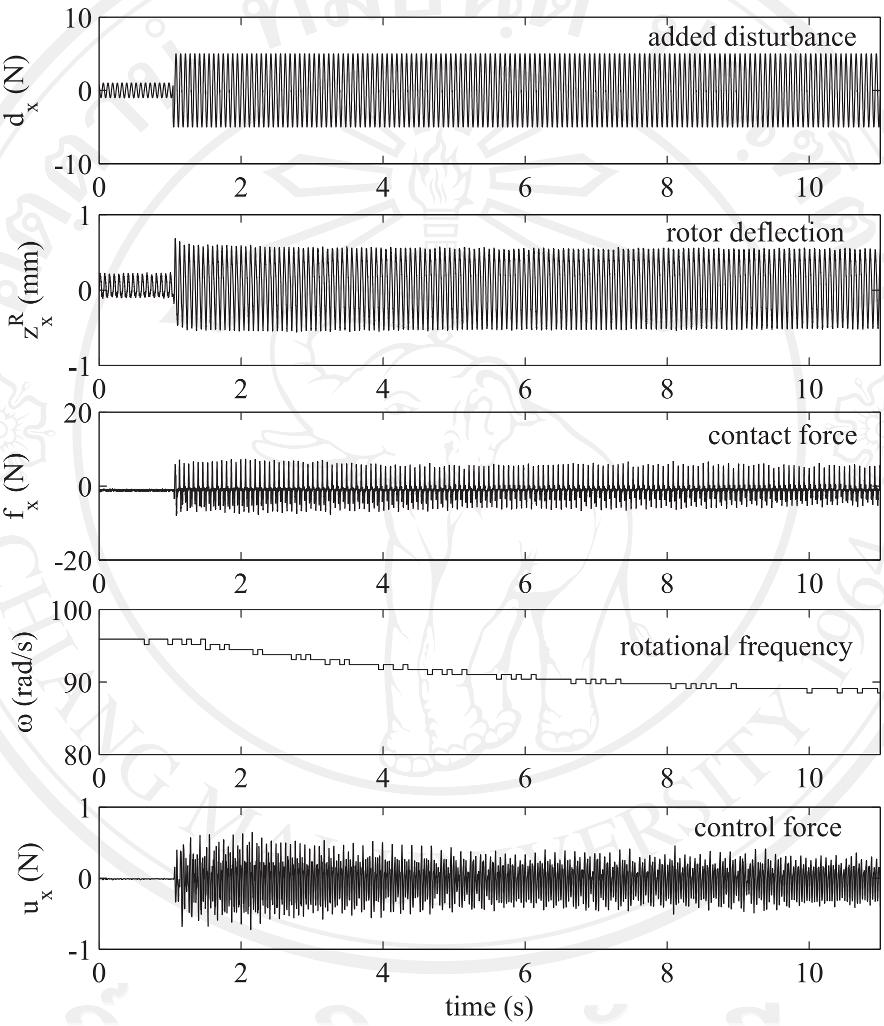

Figure 7.29: Experimental transient test at 15 Hz involving temporary increase in balance of controlled case.

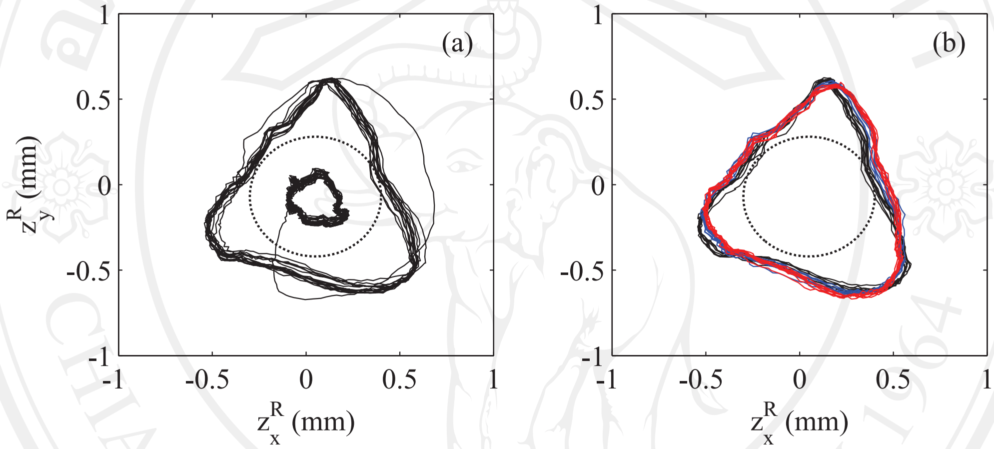

Figure 7.30: Rotor disk orbit at a contact plane operating at frequency of 15 Hz (a) Rotor orbit transition from contact free orbit to contact orbit. (b) Rotor orbit in second 2-2.5 (black), second 5-5.5(blue) and second 10-10.5(red). An initial limit of clearance is indicated by a dotted circle.